RSC Advances

ROYAL SOCIETY OF CHEMISTRY

www.rsc.org/advances

Pyrite FeS_2-C composite as a high capacity cathode material of rechargeable lithium batteries

Dat T. Tran,[a] Hong Dong,[b] Scott D. Walck,[b] and Sheng S. Zhang[*a]

[a]*Sensors and Electron Devices Directorate, U.S. Army Research Laboratory, Adelphi, MD 20783-1138, USA. Email: shengshui.zhang.civ@mail.mil; shengshui@gmail.com*

[b]*Weapons and Materials Research Directorate, U.S. Army Research Laboratory, Aberdeen Proving Ground, MD 21005-5069, USA*

Abstract

Pyrite FeS_2 is a promising cathode material for rechargeable lithium batteries because of its high theoretical capacity (894 mAh g^{-1}), low cost and near-infinite earth abundance. However, the progress in developing viable Li/FeS_2 batteries has been hampered by the poor cyclability of FeS_2 cathode. Aiming to improve the cyclability of FeS_2 cathode, we here report a facile method for the synthesis of FeS_2-C composites by an one-pot hydrothermal reaction of $FeSO_4$ and Na_2S_2 in the presence of carbon black, and examine the effect of composition on the structure of FeS_2-C composites and the cycling performance of Li/FeS_2 cells. It is shown that the added carbon not only surrounds around the FeS_2 surface but also penetrates into the entire FeS_2 particle, forming a continuously conductive network throughout the FeS_2 particle. However, introduction of carbon meanwhile increases the particle size of FeS_2 active material. These two factors lead to an improvement in the rate capability of Li/FeS_2 cells while having little effect on the specific capacity and capacity retention of FeS_2 cathode. On the other hand, we show that electrolyte plays an important role in affecting the cyclability of Li/FeS_2 cells, and that the ether- and carbonate-based electrolytes affect the cycling performance of Li/FeS_2 cells in their unique manner.

Introduction

Iron pyrite (FeS_2, also referred as to fool's gold) is an earth abundant and environmentally benign natural material that has been long used as the cathode material in commercial primary Li/FeS_2 batteries, and it is shown that Li/FeS_2 batteries have remarkable power performance and significantly longer life than other alkaline batteries.[1] Primary Li/FeS_2 batteries are based on a four-electron overall reduction of FeS_2 to metallic Fe and Li_2S with respect to a theoretical specific capacity of 894 mAh g^{-1}. Typically, Li/FeS_2 batteries have an about 1.8 V open-circuit voltage and operates at a 1.5 V averaged voltage under normal conditions. Previous effort on the primary Li/FeS_2 batteries was focused on the enhancement of FeS_2 active material utilization (i.e., accessible capacity) and rate capability by reducing the size of FeS_2 particles.[2, 3] In recent years, however, ever-increasing demand for energy storage has driven the research toward rechargeable batteries due to the low cost and near-infinite abundance of natural FeS_2 material. Up to date, a number of publications have dealt with the redox mechanism of FeS_2 at room temperature[4-8] and reported the modification of FeS_2 materials.[9-14] By the nature of conversion-type redox, FeS_2 is suitable for the cathode material of not only Li and Li-ion batteries but also Na and Na-ion batteries.[13, 15-18] Additionally, FeS_2 has also been investigated as the anode material of Li-ion and Na-ion batteries.[19-25] However, progress in developing rechargeable batteries has been hampered by the poor cyclability of FeS_2 material because of the substantially different electrochemical process of FeS_2 in the primary and rechargeable batteries. We have recognized that once being fully discharged, Li/FeS_2 batteries become a combination of a discharged Li/FeS cell and a discharged Li/S cell with the electrochemical processes as described by eqns. 1 and 2, respectively.[26]

$$Fe + Li_2S - 2e^- \leftrightarrow FeS + 2Li^+ \qquad [1]$$

$$nLi_2S - (2n-2)e^- \leftrightarrow Li_2S_n + (2n-2)Li^+ \qquad [2]$$

The strongly chemical interaction of sulfur ions in FeS and Li_2S_n results in the formation of a $FeS^{\cdots}S_nLi_2$ complex, which in some cases rearranges to produce FeS_2 as expressed by a net reaction of eqn. 3.

$$FeS + Li_2S_n \rightarrow FeS_2 + Li_2S_{n-1} \qquad [3]$$

Owing to the formation of soluble lithium polysulfide (Li_2S_n, n>2), Li/FeS_2 batteries are shown to share the same problem as those present in Li/S batteries, such as the loss of sulfur active material, redox shuttle of the dissolved Li_2S_n, and corrosion of Li anode.

On the other hand, large volume expansion (up to 255% according to the difference in molar volumes between FeS_2 and final products) accompanying with the conversion of FeS_2 to Fe and Li_2S has been identified to be the other factor to cause the performance fading of Li/FeS_2 batteries as the volume change results in ineffective contact of electrode components and inhomogeneous redistribution of electrolyte.[22] In view of material, a number of materials have been attempted to improve the cyclability of FeS_2 cathode, including FeS_2-C composites for accommodation of volume expansion,[19, 20, 27-31] micrometer- or nanometer-sized materials for high utilization (specific capacity),[13,14] novel electrolytes for excellent compatibility with the highly reactive polysulfide,[14, 17, 18, 32, 33] ionic liquids for reduced solubility of polysulfide,[34] and solid state electrolytes for complete elimination of polysulfide crossover.[35, 36] Of them, the FeS_2-C composites are of particular interest because of their advantages in simple process for synthesis, improved electric contact of FeS_2 particles with conductive carbon for high power applications, and porous structure for buffering of incurred volume expansion.

In this work we developed a facile process for the synthesis of FeS_2-C composites by a sucrose-assisted hydrothermal reaction of $FeSO_4$ and Li_2S_2 in the presence of high porous carbon black. Herein, we report that the content of carbon significantly affects the structure of FeS_2-C composites and the rate capability of Li/FeS_2 cells while having little impact on the specific capacity and capacity retention, and that the ether- and carbonate-based electrolytes affect the cycling performance of Li/FeS_2 cells in their unique manner.

Experimental

Preparation of materials

FeS_2-C composite was prepared by a one-pot hydrothermal reaction of $FeSO_4$ and Na_2S_2 in the presence of carbon black as the carbon source. In a typical process, 2.50 g (9 mmol) $FeSO_4 \cdot 7H_2O$ and 2.70 g sucrose were dissolved into 10 mL deionized water in a beaker; 2.27 g (9.45 mmol) $Na_2S \cdot 9H_2O$ and 0.288 g (9 mmol) elemental sulfur were weighed into the other beaker containing 20 mL deionized water and magnetically stirred to form a yellow-brown Na_2S_2 solution, followed by adding 0.19 g Ketjenblack EC-300JD carbon black and stirring to obtain a

homogenous carbon suspension. Preliminary FeS_2-C composite particles were obtained by adding dropwisely $FeSO_4$ solution into the resultant carbon suspension and stirring vigorously, and then was transferred into a 45 mL Teflon-lined stainless steel autoclave and heated at 180 ^oC for 18 h. After naturally cooling down to room temperature, the precipitate was collected by vacuum filtration, rinsed three times with deionized water, and finally dried under vacuum at 80 ^oC for overnight. The chemical composition and crystal structure of final product were characterized by elemental analysis, X-ray diffraction (XRD) and Raman spectroscopy, and the morphology was analyzed by Brunauer–Emmett–Teller (BET) analysis, scanning electron microscope (SEM), and scanning transmission electron microscopy (STEM). Detailed descriptions about the structural characterizations and morphological analyses are referred to the Supporting Information.

Electrode preparation and cell assembly

Resultant FeS_2-C composite powder was coated onto a carbon-coated aluminium foil at a weight ratio of 80% FeS_2-C composite, 15% Super-P carbon, and 5% binder by using poly(acrylonitrile-methyl methacrylate) (ANMMA, AN/MMA= 94:6, MW=100,000, Polysciences, Inc.) as the binder and N-methyl pyrrolidinone as the solvent. Using the same procedure, a FeS_2 electrode was prepared as the control in a composition by weight of 75% FeS_2, 10% Ketjenblack EC-300JD carbon black, 10% Super-P carbon, and 5% binder. On average, all electrodes had a loading of 2 mg FeS_2 per cm^2. The electrode was punched into 1.27 cm^2 circular discs and dried at 80 °C under vacuum for 16 h. Either an ether-based solution consisting of a 1.0 m lithium bis(trifluoromethanesulfonyl)imide (LiTFSI) dissolved in a 1:1 (wt.) mixture of dimethyl ether (DME) and 1,3-dioxolane (DOL) or a carbonate-based solution consisting of a 1.0 m $LiPF_6$ dissolved in a 3:7 (wt.) mixture of ethylene carbon (EC) and ethylmethyl carbonate (EMC) was used as the electrolyte. Using a Celgard 3410 membrane as the separator, 2032-size coin cell was assembled and filled with 18 μL electrolyte.

Electrochemical measurements

Using a Solartron SI 1287 Electrochemical Interface and a Solartron SI 1260 Impedance/Gain-Phase Analyzer, cyclic voltammetry (CV) was scanned at 0.1 mV s^{-1} between 1.0 V and 3.0 V by starting from the cell's open-circuit potential, and ac-impedance spectrum was collected at charged state over a frequency range from 100 kHz to 0.01 Hz with a 10 mV oscillation. The cell

was galvanostatically cycled between 1 V and 2.6 V on a Maccor Series 4000 cycler, and was charged at 0.5 mA cm^{-2} for all rate tests. The specific capacity was expressed by referring as to the mass of FeS_2 active material.

Results and discussion

Three FeS_2 samples having carbon content of 1.9%, 13.4% and 18.7% C, respectively, were prepared and coded as FeS_2, FeS_2-C-I, and FeS_2-C-II, of which FeS_2 was prepared as the control in the absence of carbon back. The carbon detected in FeS_2 is due to the carbon precursor coated on the surface of particles, which has been proven to be formed by the hydrothermal decomposition of sucrose.[37] The SEM images of carbon black and these three samples are displayed in Fig. 1. It can be seen that carbon black shows a porous amorphous matrix and FeS_2 consists of microcubes in size less than 1 μm (see Figs. 1a and 1b). In FeS_2-C composites (Figs. 1c and 1d), the FeS_2 particles are randomly embedded within the amorphous carbon matrix, and interestingly the FeS_2 particles are found to change in shape into microspheres and increase in size with the content of carbon. In particular, FeS_2-C-II microspheres have an averaged diameter of 2 μm. This is because carbon particles serve as the seed for nucleation of FeS_2 precipitation and the FeS_2 crystals preferentially grow from the carbon surface.

Fig. 2a shows the XRD patterns of three FeS_2 samples, which well match with the standard pyrite FeS_2 (PDF card #9000594) that has a space group of Pa3, in which the Fe atoms are octahedrally coordinated by six S atoms while the S atoms are tetrahedrally coordinated to three Fe atoms and one S atom, as illustrated by Fig. 2b. The Raman spectra of carbon black, FeS_2 and FeS_2-C-II are compared in Fig. 2c. Obviously, FeS_2-C-II combines the characteristics of FeS_2 and carbon black, including two relatively strong peaks at 363 and 375 cm^{-1} and a very weak peak at 433 cm^{-1} for the S_2 vibration (E_g), S−S in-phase stretch (A_g), and coupled vibration and stretch (T_g) modes of pyrite FeS_2,[38, 39] and two strong peaks at 1349 and 1593 cm^{-1} for the disorder-induced D-band and graphite structure-derived G-band of carbon materials.[40] There is an additional broad peak at 1100-1680 cm^{-1} in the control FeS_2, which is due to the carbon precursor coated on the surface of FeS_2 particles as suggested by the 1.9% C in FeS_2. Fig. 2d shows the SEM image of a typical FeS_2-C-II microsphere, indicating that the surface of FeS_2 microsphere in FeS_2-C-II is composed of tightly assembled nanorods with a diameter of about 40 nanometers and that amorphous carbon randomly surrounds around the FeS_2 microsphere.

Chemical composition of FeS_2-C-II composite is further analyzed by acquiring an X-ray energy dispersive spectroscopy (XEDS) spectrum image in the scanning transmission electron microscopy (STEM) and analyzing the data with an automated eXpert spectral image analysis (AXSIA) software.[41, 42] The results are summarized in Fig. 3, in which Fig. 3a shows the cross section of a FeS_2-C-II microsphere prepared by ultramicrotomy using high angle annular dark field (HAADF) imaging and Fig. 3b shows three main component phases by color of the interested cross section. The green, red, and blue colors in Fig. 3b are identified to be the carbon, FeS_2 with a small amount of carbon, and FeS_2 phase, respectively, by the XEDS component spectra as indicated in Fig. 3c. The carbon (green color) surrounding around the FeS_2-C-II particle arises from the epoxy resin that was used to hold the particle in the STEM experiment, whereas those distributing over the entire particle, as indicated by the red color, are the added carbon black that connects together to form a continuously conductive network. The SEM images (Figs. 1c, 1d, and 2d) and STEM image (red color in Fig. 3b) distinctly demonstrate that the added carbon black not only surrounds around the surface of FeS_2 microspheres but also penetrates throughout the particle. The formed conductive carbon network must benefit to the rate capability of FeS_2 cathode.

Fig. 4 shows the basic electrochemical properties of FeS_2 cathode measured in an ether-based electrolyte and a carbonate-based electrolyte, respectively. In both types of electrolytes, FeS_2 presents a major cathodic current peak starting at ~1.5 V vs. Li/Li^+ in the first CV scanning (see Figs. 4a and 4c) and a voltage plateau at ~1.5 V in the first discharge (see Figs. 4b and 4d). These results agree with a number of previous publications, and are attributed to two equal-capacity solid-solid phase transitions as described by eqns. 4 and 5.[3-6]

$$FeS_2 + 2Li \rightarrow Li_2FeS_2 \qquad [4]$$

$$Li_2FeS_2 + 2Li \rightarrow Fe + Li_2S \qquad [5]$$

However, these two electrochemical processes cannot be visually distinguished in the CV and discharging voltage curve because of their close operation voltages. In recharge, the Li/FeS_2 cell behaves as a combination of a discharged Li/FeS cell and a discharged Li/S cell. Consequently, the cell shows two distinct electrochemical processes relating to eqn. 1 and eqn.2, respectively, as indicated by two anodic current peaks at 1.96 V and 2.60 V in CV and two voltage plateaus at 1.86 V and 2.45 V in recharge. Significant differences in electrochemical behavior between two

types of electrolytes are observed from the 1st recharge and 2nd discharge. In the 1st recharge, the ether-based electrolyte cell suffers slight redox shuttle at 2.5 V (see Fig. 4b); In the 2nd discharge, the ether-based electrolyte cell has much lower currents in the 2.0 V cathodic peak (Fig. 4a vs. 4c) and larger capacity loss from the 1st to 2nd discharge (Fig. 4b vs. 4d). All these differences consistently suggest the dissolution of Li_2S_n and resulting loss of sulfur active material in the ether-based electrolyte, namely the same problems as those present in the Li/S batteries. It is well known that carbonate-based electrolytes are chemically incompatible with Li/S batteries because of the nucleophilic reaction between the carbonate solvents and Li_2S_n.[43-45] Herein, the ability of FeS_2 cathode operating in a carbonate-based electrolyte is attributed to the formation of a complex between the solid FeS and the Li_2S_n dissolved in electrolyte, i.e. a chemical adsorption, which greatly reduces the reactivity of Li_2S_n.

Fig. 5a shows the effect of electrolytes on the capacity retention of Li/FeS_2 cells with three different FeS_2 cathodes. With both types of electrolytes, the cells delivers a 810~900 mAh g^{-1} capacity, equaling to a 90~100% of the theoretical capacity, in the first discharge. It is indicated by comparing Fig. 4b and 4d that from the 1st discharge to 2nd discharge, the ether-based electrolyte cell loses more capacities than the carbonate-based counterpart. This is because Li_2S_n has much higher solubility in the ether solvents than in the carbonate solvents, resulting in larger loss of sulfur active material. However, the ether-based electrolyte cells remain better capacity retention, and particularly two types of cells reach similar capacities after ~50 cycles (Fig. 5a). The faster capacity fading rate of the carbonate-based electrolyte cells suggests that slow reactions between the carbonate solvents and Li_2S_n are still present although the reactivity of Li_2S_n has been greatly weakened by the chemical adsorption of FeS. In order to further understand the effect of electrolytes, the voltage curves of the 46th cycle at which two Li/FeS_2 cells with the ether- and carbonate-based electrolytes had the same capacity (440 mAh g^{-1}) are plotted and compared with those of the 2nd cycle in Fig. 5b. It can be clearly observed that the plateau feature entirely disappeared from the discharge voltage profile of the ether-based electrolyte cell, suggesting that the Li anode had been severely polarized by the insoluble reaction products (mainly Li_2S and Li_2S_2) of metallic Li and dissolved Li_2S_n. The above results reveal that the cycling performance of Li/FeS_2 cells is affected by the ether- and carbonate-based electrolytes in their unique manner, i.e., by the dissolution of Li_2S_n in the ether-based electrolytes

and by the nucleophilic reaction between the solvent and Li_2S_n in the carbonate-based electrolytes.

Additionally, it can be seen from Fig. 5a that the composition of FeS_2-C composites affects the cycling performance of Li/FeS_2 cells differently in the ether- and carbonate-based electrolytes. With an increase in the carbon content of the FeS_2-C composites, the specific capacity of FeS_2 slightly increases in the ether-based electrolyte while remaining unchanged in the carbonate-based electrolyte. This is because in the ether-based electrolyte, the highly porous carbon helps to trap the dissolved Li_2S_n from diffusing out of the cathode by physical absorption, whereas in the carbonate-based electrolyte, this effect is masked by the low solubility of Li_2S_n. In both types of electrolytes, however, the composition of the FeS_2-C composite seems not to affect the capacity retention of Li/FeS_2 cells as suggested by the fact that all these cells with the same electrolyte experience the similar capacity fading rate. Less significant effect of the carbon content on the capacity retention of the FeS_2 cathode is because the introduction of carbon black increases the size of FeS_2 microspheres as indicated in Fig. 1, which consequently reduces the utilization of FeS_2 active materials.

Fig. 6 indicates the effect of charging cutoff voltage on the cycling performance of Li/FeS_2-C-II cells. When cutting off at 2.3 V, namely right before the 2.5 V voltage plateau appears, the cell has lower capacity but leads to much stable capacity retention. The similar phenomenon has also been observed from Li/FeS cells with an ether-based electrolyte.[37] This is because no long-chain (soluble) Li_2S_n can be formed at or lower than 2.3 V. Therefore, the improved capacity retention by the 2.3 V charging cutoff voltage can be attributed to the reduced reactivity of the short-chain Li_2S_n for the carbonate-based electrolyte cell and to the low solubility of the short-chain Li_2S_n for the ether-based electrolyte cell.

Fig. 7a compares the rate capability of two cells using FeS_2 and FeS_2-C-II, respectively, as the cathode material and a carbonate-based electrolyte. In order to access to the full capacity, all charging processes were performed at 0.5 mA cm^{-2}. It was observed that all cycles had near 100% coulombic efficiencies although the cell was charged and discharged at different current densities. It can be seen from Fig. 7a that two cells have the similar capacities when the current density is lower than 1.0 mA cm^{-2}, and that the cell with FeS_2-C-II cathode outperforms once the current density exceeds 1.0 mA cm^{-2}. Fig. 7b shows the discharge voltage curves of the cell at

different current densities. As normal, the voltage and capacity are declined with an increase in the discharging current density. The former is due to the IR drop in which the R includes both of the ohmic resistance and faradic resistance, and the latter relates to the increased ionic concentration polarization as well as the limited electrode reaction kinetics. As indicated by the voltage curves at 2.5 and 3.0 mA cm^{-2} in Fig. 7b, the lower voltage plateau cannot reach the end before the voltage declines to the cutoff voltage (1.0 V) because of the significant IR drop.

Impedance analysis was used to understand the effect of carbon content on the rate capability of the FeS_2-C cathode. Fig. 8 compares the impedance spectra of two cells with the FeS_2 and FeS_2-C-II cathodes, respectively, which were collected at fully charged state by charging the cell to 2.6 V and keeping it at 2.6 V until the current density declines to 0.1 mA cm^{-2}. As normal, the impedance spectra of both cells show two overlapped semicircles followed by a straight slopping line in the low frequency end, which briefly reflect the ohmic resistance (R_{sl}) of the electrolyte-electrode interface and the faradic charge-transfer resistance (R_{ct}) of the electrode reaction. The R_{sl} and R_{ct} are two important elements of the impedance spectrum of a solid electrode, and can be fit using an equivalent circuit as shown by the inset in Fig. 8.[46, 47] It can be seen from Fig. 8 that these two cells have almost the same bulk resistance (R_b), however, the one with the FeS_2-C-II cathode has lower R_{sl} and R_{ct}. This observation verifies that the FeS_2-C composite forms higher conductive electrolyte-electrode interface and offers faster electrode reaction kinetics, providing an excellent endorsement for the better rate capability observed from Fig. 7a.

Conclusions

In summary, we developed a facile process for the synthesis of FeS_2-C composites by a one-pot hydrothermal reaction of $FeSO_4$ and Na_2S_2 in the presence of carbon. A wide range of resources for commercial carbon materials provide great flexibility for architectural design and property modification of the FeS_2-C composite materials. The results of the present work show that the cyclability of FeS_2 cathode is affected by the FeS_2-C composite in multiple aspects, including (1) the particle size of FeS_2 active material, which is found to increase with the carbon content in the composite, (2) the physical absorption of carbon surface to Li_2S_n, which helps to trap the dissolved Li_2S_n from diffusing out of the cathode, and (3) the formation of a conductive carbon network, which increases rate capability of the battery. In addition, the type of electrolytes is

shown to play an important role in affecting the cyclability of FeS_2 cathode. Briefly, the cyclability of the Li/FeS_2 batteries is affected by the ether-based electrolytes through the dissolution of lithium polysulfide and by the carbonate-based electrolyte through the parasitic reaction between the carbonate solvent and polysulfide anions.

Notes and references

1. D. Linden, T.B. Reddy, Handbook of Batteries, 3rd ed., McGraw-Hill, Inc., 2002, Chapter 14.
2. Y. Shao-Horn, S. Osmialowski and Q. C. Horn, *J. Electrochem. Soc.*, 2002, **149**, A1499−A1502.
3. Y. Shao-Horn, S. Osmialowski and Q. C. Horn, *J. Electrochem. Soc.*, 2002, **149**, A1547−A1555.
4. R. Fong, J. R. Dahn and C. H. W. Jones, *J. Electrochem. Soc.*, 1989, **136**, 3206−3210.
5. R. Brec, E. Prouzet and G. Ouvrard, *J. Power Sources*, 1989, **26**, 325−332.
6. D. A. Totir, I. T. Bae, Y. N. Hu, M. R. Antonio, M. A. Stan and D. A. Scherson, *J. Phys. Chem. B*, 1997, **101**, 9751−9756.
7. E. Strauss, D. Golodnitsky and E. Peled, *Electrochim. Acta*, 2000, **45**, 1519−1525.
8. L. A. Montoro, J. M. Rosolen, J. H. Shin and S. Passerini, *Electrochim. Acta*, 2004, **49**, 3419−3427.
9. E. Peled, D. Golodnitsky, E. Strauss, J. Lang and Y. Lavi, *Electrochim. Acta*, 1998, **43**, 1593−1599.
10. D. Zhang, J. P. Tu, J. Y. Xiang, Y. Q. Qiao, X. H. Xia, X. L. Wang and C. D. Gu, *Electrochim. Acta*, 2011, **56**, 9980−9985.
11. T. Takeuchi, H. Kageyama, K. Nakanishi, Y. Inada, M. Katayama, T. Ohta, H. Senoh, H. Sakaebe, T. Sakai, K. Tatsumi and H. Kobayashi, *J. Electrochem. Soc.*, 2012, **159**, A75−A84.
12. L. Li, M. Caban-Acevedo, S. N. Girard and S. Jin, *Nanoscale*, 2014, **6**, 2112−2118.
13. M. Walter, T. Zund and M. V. Kovalenko, *Nanoscale*, 2015, **7**, 9158−9163.
14. Z. Hu, K. Zhang, Z. Zhu, Z. Tao and J. Chen, *J. Mater. Chem. A*, 2015, **3**, 12898−12904.
15. T. B. Kim, J. W. Choi, H. S. Ryu, G. B. Cho, K. W. Kim, J. H. Ahn, K. K. Cho and H. J. Ahn, *J. Power Sources*, 2007, **174**, 1275−1278.
16. A. Kitajou, J. Yamaguchi, S. Hara and S. Okada, *J. Power Sources*, 2014, **247**, 391−395.
17. Y. Zhu, L. Suo, T. Gao, X. Fan, F. Han and C. Wang, *Electrochem. Commun.*, 2015, **54**, 18−22.
18. Z. Hu, Z. Zhu, F. Cheng, K. Zhang, J. Wang, C. Chen and J. Chen, *Energy Environ. Sci.*, 2015, **8**, 1309−1316.
19. B. Wu, H. Song, J. Zhou and X. Chen, *Chem. Commun.*, 2011, **47**, 8653−8655.
20. D. Zhang, Y. J. Mai, J. Y. Xiang, X. H. Xia, Y. Q. Qiao and J. P. Tu, *J. Power Sources*, 2012, **217**, 229−235.
21. D. Zhang, G. Wu, J. Xiang, J. Jin, Y. Cai and G. Li, *Mater. Sci. Eng. B*, 2013, **178**, 483−488.
22. J. Xia, J. Jiao, B. Dai, W. Qiu, S. He, W. Qiu, P. Shen and L. Chen, *RSC Adv.*, 2013, **3**, 6132−6140.
23. W. Qiu, J. Xia, H. Zhong, S. He, S. Lai and L. Chen, *Electrochim. Acta*, 2014, **137**, 197−205.

24. X. Wen, X. Wei, L. Yang and P. K. Shen, *J. Mater. Chem. A*, 2015, **3**, 2090−2096.
25. H. Xue, D. Y. W. Yu, J. Qing, X. Yang, J. Xu, Z. Li, M. Sun, W. Kang, Y. Tang and C. S. Lee, *J. Mater. Chem. A*, 2015, **3**, 7945−7949.
26. S. S. Zhang, *J. Mater. Chem. A*, 2015, **3**, 7689−7694.
27. L. Liu, Z. Yuan, C. Qiu and J. Liu, *Solid State Ionics*, 2013, **241**, 25−29.
28. J. Liu, Y. Wen, Y. Wang, P. A. van Aken, J. Maier and Y. Yu, *Adv. Mater.*, 2014, **26**, 6025−6030.
29. S. B. Son, T. A. Yersak, D. M. Piper, S. C. Kim, C. S. Kang, J. S. Cho, S. S. Suh, Y. U. Kim, K. H. Oh and S. H. Lee, *Adv. Energy Mater.*, 2014, **4**, 1300961.
30. T. S. Yoder, M. Tussing, J. E. Cloud and Y. Yang, *J. Power Sources*, 2015, **274**, 685−692.
31. T. S. Yoder, M. Tussing, J. E. Cloud and Y. Yang, *ECS Meeting Abstracts*, 2014, **2**, No. 257.
32. L. A. Montoro and J. M. Rosolen, *Solid State Ionics*, 2003, **159**, 233−240.
33. J. W. Choi, G. Cheruvally, H. J. Ahn, K. W. Kim and J. H. Ahn, *J. Power Sources*, 2006, **163**, 158−165.
34. T. Evans, D. M. Piper, S. C. Kim, S. S. Han, V. Bhat, K. H. Oh and S. H. Lee, *Adv. Mater.*, 2014, **26**, 7386−7392.
35. T. A. Yersak, H. A. Macpherson, S. C. Kim, V. D. Le, C. S. Kang, S. B. Son, Y. H. Kim, J. E. Trevey, K. H. Oh, C. Stoldt and S. H. Lee, *Adv. Energy Mater.*, 2013, **3**, 120−127.
36. V. Pelé, F. Flamary, L. Bourgeois, B. Pecquenard and F. Le Cras, *Electrochem. Commun.*, 2015, **51**, 81−84.
37. D. T. Tran and S. S. Zhang, *J. Mater. Chem. A*, 2015, **3**, 12240−12246.
38. H. Vogt, T. Chattopadhyay and H. J. Stolz, *J. Phys. Chem. Solids*, 1983, **44**, 869−873.
39. A. K. Kleppe and A. P. Jephcoat, *Mineral. Mag.*, 2004, **68**, 433−441.
40. M. A. Pimenta, G. Dresselhaus, M. S. Dresselhaus, L. G. Cancado, A. Jorio and R. Saito, *Phys. Chem. Chem. Phys.*, 2007, **9**, 1276−1290.
41. P. G. Kotula, M. R. Keenan and J. R. Michael, *Microsc. Microanal.*, 2003, **9**, 1−17.
42. M. R. Keenan and P. G. Kotula, *Surf. Interface Anal.*, 2004, **36**, 203−212.
43. J. Gao, M. A. Lowe, Y. Kiya and H. D. Abruna, *J. Phys. Chem. C*, 2011, **115**, 25132−25137.
44. T. Yim, M. S. Park, J. S. Yu, K. J. Kim, K. Y. Im, J. H. Kim, G. Jeong, Y. N. Jo, S. G. Woo, K. S. Kang, I. Lee and Y. J. Kim, *Electrochim. Acta*, 2013, **107**, 454−460.
45. S. S. Zhang, *J. Power Sources*, 2013, **231**, 153−162.
46. S. S. Zhang, K. Xu and T. Jow, *J. Electrochem. Soc.*, 2002, **149**, A1521−A1526.
47. S. S. Zhang, K. Xu and T. R. Jow, *Electrochim. Acta*, 2002, **48**, 241−246.

Figure captions

Figure 1. SEM images of (a) carbon black, (b) FeS_2, (c) FeS_2-C-I, and (d) FeS_2-C-II.

Figure 2. Structural characterizations of FeS_2-C composite. (a) XRD pattern, (b) schematic representation of a pyrite FeS_2 unit cell, (c) Raman spectrum, and (d) SEM image of a FeS_2-C-II composite particle.

Figure 3. STEM X-ray microanalysis of the cross-section of a FeS_2-C-II particle. (a) HAADF image, (b) map of three main component phases, and (c) EDS component spectra of each main phase in (b) where the green, red and blues colors represent the carbon, FeS_2 with a small amount of carbon, and FeS_2 phase, respectively.

Figure 4. Cyclic voltammogram and voltage profile of the first two cycles of Li/FeS_2 cells with different types of electrolytes. (a) and (b): 1.0 m $LiSO_3CF_3$ 1:1 DME/DOL; (c) and (d): 1.0 m $LiPF_6$ 3:7 EC/EMC.

Figure 5. Effect of electrolytes on the cycling performance of Li/FeS_2 cells. (a) Capacity retention, and (b) voltage curve in the 2nd and 46th cycles.

Figure 6. Influence of charging cutoff voltage on capacity retention of Li/FeS_2 cells.

Figure 7. Rate capability of Li/FeS_2 cells with a 1.0 m $LiPF_6$ 3:7 EC/EMC electrolyte. (a) Comparison of FeS_2 and FeS_2-C-II cathodes, and (b) discharging voltage curves of a Li/FeS_2-C-II cell at different current densities.

Figure 8. Impedance spectra of two Li/FeS_2 cells with FeS_2 and FeS_2-C-II cathodes, respectively, collected at charged state, in which the inset shows an equivalent circuit suitable for fitting of the impedance spectra.

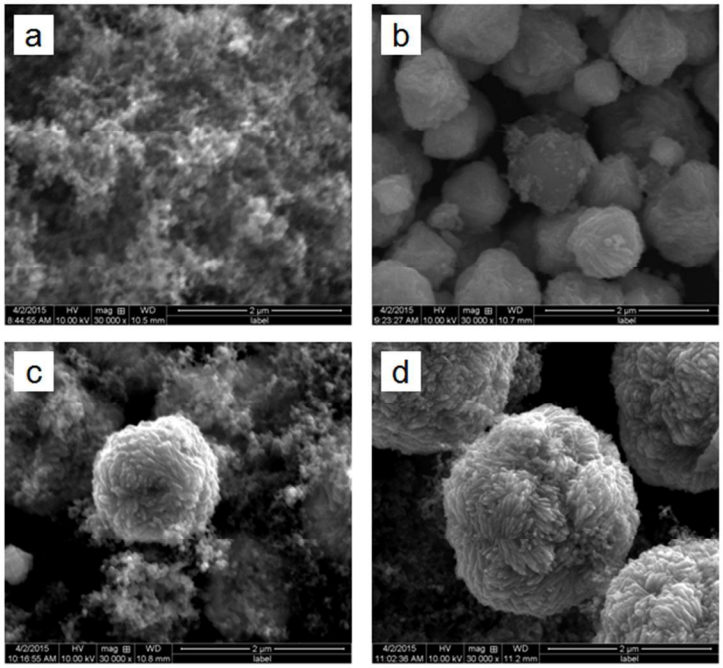

Figure 1. SEM images of (a) carbon black, (b) FeS_2, (c) FeS_2-C-I, and (d) FeS_2-C-II.

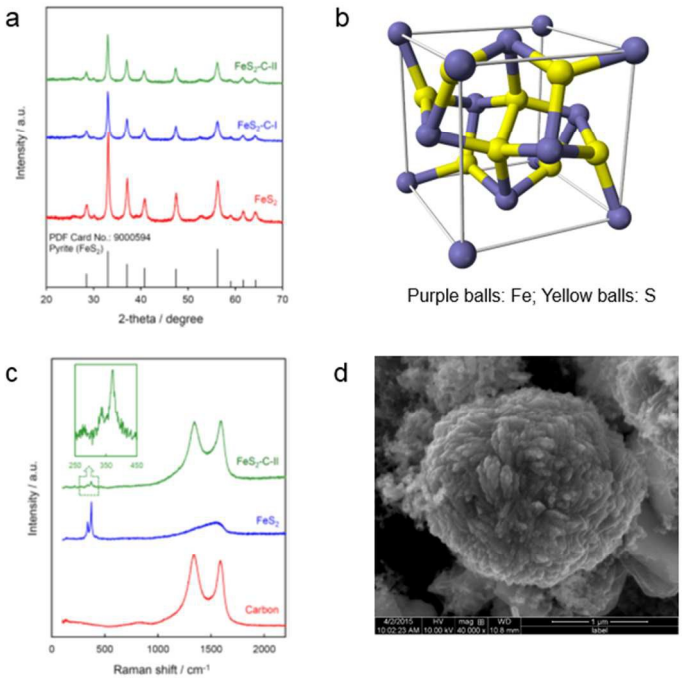

Figure 2. Structural characterizations of FeS_2-C composite. (a) XRD pattern, (b) schematic representation of a pyrite FeS_2 unit cell, (c) Raman spectrum, and (d) SEM image of a FeS_2-C-II composite particle.

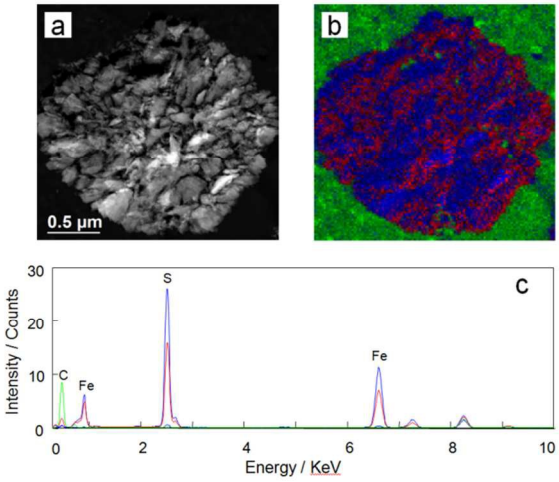

Figure 3. STEM analysis on the cross-section of a FeS_2-C-II particle. (a) HAADF image, (b) map of three main compositions, and (c) EDS spectra of each main composition in (b) where the green, red and blues colors represent carbon, FeS_2 with a small amount of carbon, and FeS_2, respectively.

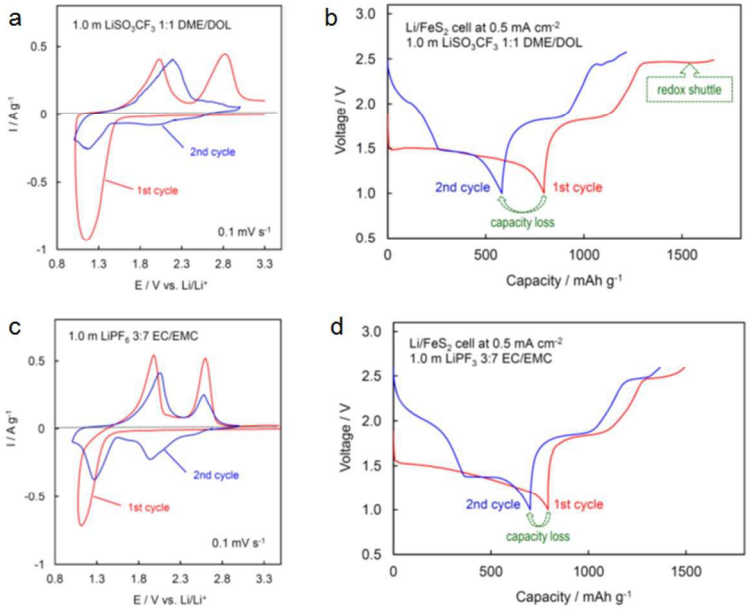

Figure 4. Cyclic voltammogram and voltage profile of the first two cycles of Li/FeS_2 cells with different types of electrolytes. (a) and (b): 1.0 m $LiSO_3CF_3$ 1:1 DME/DOL; (c) and (d): 1.0 m $LiPF_6$ 3:7 EC/EMC.

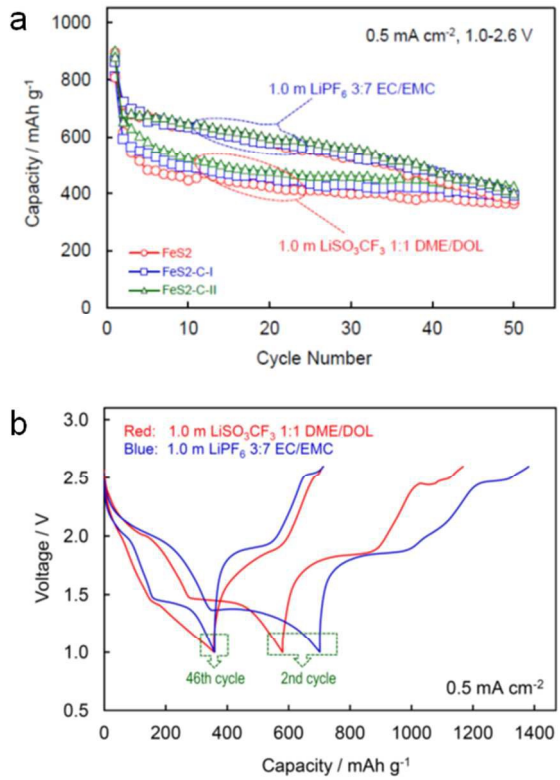

Figure 5. Effect of electrolytes on the cycling performance of Li/FeS_2 cells. (a) Capacity retention, and (b) voltage curve in the 2nd and 46th cycles.

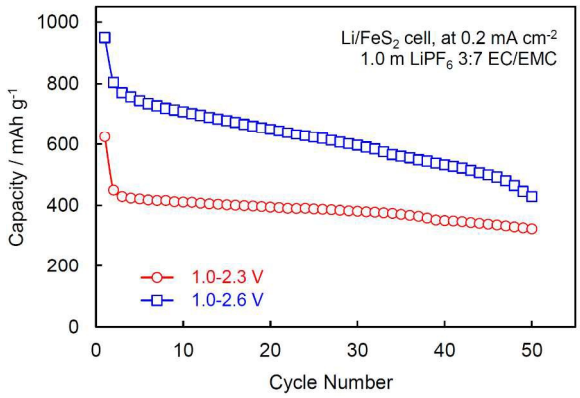

Figure 6. Influence of charging cutoff voltage on capacity retention of Li/FeS_2 cells.

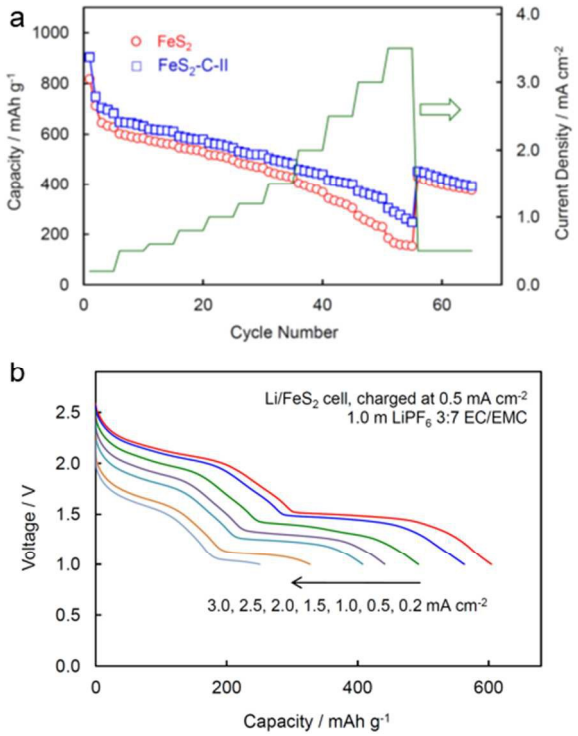

Figure 7. Rate capability of Li/FeS_2 cells with a 1.0 m $LiPF_6$ 3:7 EC/EMC electrolyte. (a) Comparison of FeS_2 and FeS_2-C-II cathodes, and (b) discharging voltage curves of a Li/FeS_2-C-II cell at different current densities.

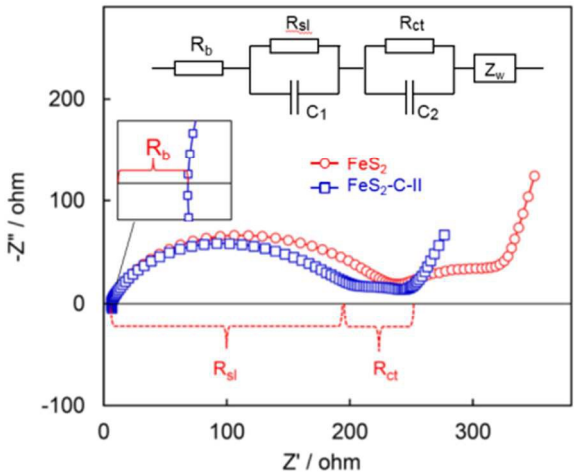

Figure 8. Impedance spectra of two Li/FeS_2 cells with FeS_2 and FeS_2-C-II cathodes, respectively, collected at charged state, in which the inset shows an equivalent circuit suitable for fitting of the impedance spectra.